

An investigation into the effects of voids, inclusions and minor cracks on major crack propagation by using XFEM

Shouyan Jiang^{*1,2}, Chengbin Du^{2a} and Chongshi Gu^{1b}

¹College of Water Conservancy and Hydropower Engineering, Hohai University, Nanjing 210098, China

²College of Mechanics and Materials, Hohai University, Nanjing 210098, China

(Received February 24, 2013, Revised December 20, 2013, Accepted January 27, 2014)

Abstract. For the structures containing multiple discontinuities (voids, inclusions, and cracks), the simulation technologies in the framework of extended finite element method (XFEM) are discussed in details. The level set method is used for representing the location of inner discontinuous interfaces so that the mesh does not need to align with these discontinuities. Several illustrations have been given to verify that the implemented XFEM program is effective. Then, the implemented XFEM program is used to investigate the effects of the voids, inclusions, and minor cracks on the path of major crack propagation. For a plate containing cracks and voids, two possibly crack path can be observed: i) the crack propagates into the void; ii) the crack initially curves towards the void, then, the crack reorients itself and propagates along its original orientation. For a plate with a soft inclusion, the final predicted crack paths tend to close with the inclusion, and an evident difference of crack paths can be observed with different inclusion material properties. However, for a plate with a hard inclusion, the paths tend to away from the inclusion, and a slightly difference of crack paths can only be seen with different inclusion material properties. For a plate with several minor cracks, the trend of crack paths can still be described as that the crack initially curves towards these minor cracks, and then, the crack reorients itself and propagates almost horizontally along its original orientation.

Keywords: extended finite element method; crack propagation; voids; inclusions; cracks

1. Introduction

The standard finite element method (FEM) provides substantial advantages in dealing with continuous problems. However, for discontinues problems, it is computationally expensive to obtain accurate solutions in the FEM approximations: the mesh has to align with a discontinuity and a considerable mesh refinement is required around a discontinuous feature. The extended finite element method (XFEM) was first introduced by Belytschko and Black (1999), based on the idea of the partition of unity approach (Melenk and Babuška 1996). The XFEM ameliorates the drawbacks of the FEM mentioned above in solving discontinues problems. Therefore, the XFEM is widely used in many fields as soon as the method is introduced, such as fracture mechanics,

*Corresponding author, Post-doctoral, E-mail: syjiang@hhu.edu.cn

^aProfessor, E-mail: cbdu@hhu.edu.cn

^bProfessor, E-mail: csgu@hhu.edu.cn

flow fields (Liao and Zhuang 2012), contact (Mayer *et al.* 2010), composites (Dréau *et al.* 2010), and so on. The XFEM approximation consists of standard finite elements which are used in the major part of the domain and enriched elements in the enriched sub-domain for capturing special solution properties such as discontinuities and singularities. The goal of using enriched elements in the standard XFEM is to expand the approximation function space of the standard FEM such that the enriched approximation can cover or closer to the exact solution. Therefore, the XFEM is a powerful tool for simulating discontinuous problems.

Additionally, composite materials have attracted considerable interest due to potential to achieve a better performance, such as concrete composites (Du *et al.* 2012). Due to the nature of composite materials, multiple discontinuities will be contained in the structure when investigating the mechanical behavior of the structure. A few studies have been carried out for the modeling and simulation of several discontinuities. Yan and Park (2008) applied the XFEM for the simulation of near-interfacial crack propagation in a metal-ceramic layered structure. Singh *et al.* (2011) investigated the influences of number of voids/inclusions in the domain on the change in the stress intensity factor (SIF) of the main crack. Later, Singh *et al.* (2012) also evaluated the fatigue life of structures/components having multiple discontinuities such as holes, cracks and inclusions. Kim *et al.* (2011) analyzed the effect of equivalent initial flaw size distribution on a multiple site damage specimen. Chang *et al.* (2012) investigated the effect of reinforcing particles on the crack propagation behavior and fatigue performance during cyclic loading. Haboussa *et al.* (2011) was devoted to the crack-hole interaction problem. However, the simulation of crack propagation is still a challenging task especially when microscale/mesoscale structures are concerned. Sun *et al.* (2013) developed a novel algorithm based on the XFEM and an enhanced artificial bee colony algorithm to detect and quantify multiple flaws in structures. Wu and Wong (2013) investigated the effects of weak and stiff circular inclusions on the overall mechanical behavior, in particular the cracking processes (crack initiation, propagation and coalescence) of a rectangular rock mass under uniaxial compression. The outcome of this study can improve the understanding of the effects of voids, inclusions, and minor cracks on the major crack propagation paths.

The aim of this paper is to investigate the effects of voids, inclusions, and minor cracks on the major crack propagation paths by developing XFEM. For the structures containing multiple discontinuities (voids, inclusions, and cracks), the simulation technologies in the framework of XFEM are discussed in details. The emphasis are paid on the selections of enrichment functions, the numerical integrations at the discontinuities, the evaluations of the SIF, as well as the criterion of crack propagation while the XFEM is used to study the mechanical behaviors of the structure containing the geometric and/or physical discontinuities. The level set method (LSM) is used for representing the location of inner discontinuous interfaces containing the boundaries of voids and inclusions, and the surface of cracks, so that the mesh does not need to align with these discontinuities. The governing equation for XFEM is deduced. Several illustrations have been given to verify that the implemented XFEM program is effective for modeling voids, inclusions, and crack propagation. Then, the implemented XFEM program is used to investigate the effects of the voids, inclusions, and minor cracks on the path of major crack propagation.

2. Geometric description of voids, inclusions, and cracks

2.1 Geometric description of voids and inclusions

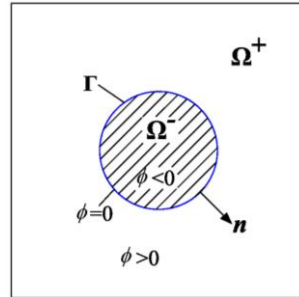


Fig. 1 Domain with a circular interface

A powerful tool for tracking interfaces is the LSM (Osher and Sethian 1988). In LSM, the interface of interest is represented as the zero level set of a function, $\phi(\mathbf{x})$. This function is one dimension higher than the dimension of the interface.

Consider a domain, Ω , divided into two non-overlapping subdomains, Ω^+ and Ω^- , sharing a circular interface, Γ , as illustrated in Fig. 1. On Ω^+ , the level set function $\phi(\mathbf{x}) > 0$; on Ω^- , the level set function $\phi(\mathbf{x}) < 0$; on Γ , $\phi(\mathbf{x}) = 0$.

The circular level set function can be expressed as (Sukumar *et al.* 2001)

$$\phi(\mathbf{x}) = \min_{i=1,2,\dots,n_c} \{ \|\mathbf{x} - \mathbf{x}_i^c\| - r_i^c \} \quad (1)$$

where, n_c is the number of circular voids/inclusions, and \mathbf{x}_i^c is the location of the centre of the i th circular void/inclusion with the radius of r_i^c .

In the discretized domains, the values of the level set functions are stored only at the nodes, that is $\phi_i = \phi(\mathbf{x}_i)$. The level set values can be interpolated over the mesh by

$$\phi^h(\mathbf{x}) = \sum_i N_i(\mathbf{x}) \phi_i \quad (2)$$

where $N_i(\mathbf{x})$ is the standard finite element shape functions.

2.2 Geometric description of cracks

Two level sets $\psi(\mathbf{x}, t)$ and $\phi^k(\mathbf{x}, t)$ ($k=1, 2$) are used to describe the crack. As shown in Fig. 2, the functions are written as ψ and ϕ^k in the simplified form. The crack tip level set ϕ^k is generally assumed to be orthogonal to ψ . The function $\psi(\mathbf{x}, t)$ can be expressed by the signed distance function, that is

$$\psi(\mathbf{x}, t) = \|\mathbf{x} - \mathbf{x}^*\| \text{sign}((\mathbf{x} - \mathbf{x}^*) \cdot \mathbf{n}) \quad (3)$$

where, \mathbf{x} is the coordinate of the point P ; \mathbf{x}^* is the projection of the point P on the crack surface; \mathbf{n} is the unit outward normal to the crack surface; $\text{sign}(x)$ is the signed function; $\text{sign}(x) = 1$ for $x > 0$; $\text{sign}(x) = 0$ for $x = 0$; and $\text{sign}(x) = -1$ for $x < 0$.

The function, $\phi^k(\mathbf{x}, t)$, can be defined as

$$\phi^k(\mathbf{x}, t) = (\mathbf{x} - \mathbf{x}_k) \cdot \mathbf{t} \quad (4)$$

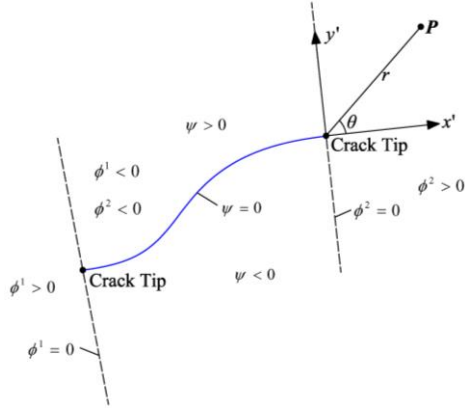


Fig. 2 Crack description by two level set functions

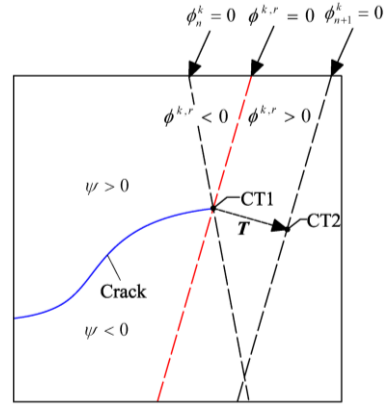


Fig. 3 Update of the level set functions

where \mathbf{x}_k is the coordinate of the k th crack tip and \mathbf{t} is the unit tangential vector at the k th crack tip.

The values of the level set functions are stored only at the nodes as in the previous case. The level set values can be interpolated over the mesh by (Stolarska and Chopp 2003)

$$\begin{cases} \phi^k(\mathbf{x}, t) = \sum_i N_i(\mathbf{x})(\phi^k(\mathbf{x}_i, t)), \\ \psi(\mathbf{x}, t) = \sum_i N_i(\mathbf{x})\psi_i(\mathbf{x}, t) \end{cases} \quad (5)$$

Crack growth is modeled by appropriately updating the ϕ^k and ψ functions. The evolution of the level set functions ϕ^k and ψ is determined by the crack growth direction θ_c . As shown in Fig. 3, in each step, the displacement vector of the crack tip is $\mathbf{T}=(T_x, T_y)$. The coordinate of the crack tip CT1 is (x_1, y_1) , and the coordinate of the crack tip CT2 is (x_2, y_2) . The following steps describe the procedure of the evolution of the level set functions ϕ_n^k and ψ_n at the step n , that is to compute the level set functions ϕ_{n+1}^k and ψ_{n+1} at the step $n+1$.

Step 1: Compute the rotated level set $\phi^{k,r}$ of ϕ_n^k , and $\phi^{k,r}$ at the node with the coordinate of (x, y) can be given by

$$\phi^{k,r} = (x - x_1) \frac{T_x}{\|\mathbf{T}\|} + (y - y_1) \frac{T_y}{\|\mathbf{T}\|} \quad (6)$$

Step 2: Compute the level set ψ_{n+1} . If $\phi^{k,r} < 0$, the level set ψ_{n+1} will not be updated, that is $\psi_{n+1} = \psi_n$. If $\phi^{k,r} > 0$, ψ_{n+1} can be computed by

$$\psi_{n+1} = \pm \left| (x - x_1) \frac{T_y}{\|\mathbf{T}\|} + (y - y_1) \frac{T_x}{\|\mathbf{T}\|} \right| \quad (7)$$

Step 3: Compute the level set ϕ_{n+1}^k , and ϕ_{n+1}^k can be given by

$$\phi_{n+1}^k = \phi_n^k - \|\mathbf{T}\| \quad (8)$$

At a point \mathbf{x} , the polar coordinate r and θ with respect to the tangent to the crack tip are defined as

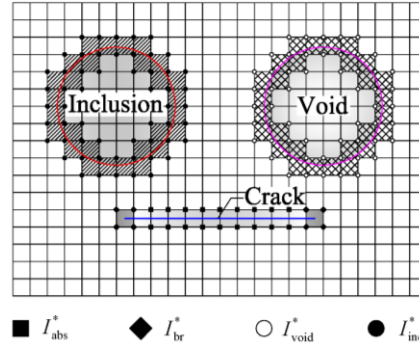


Fig. 4 Discretized domains in two dimensions with nodal subsets I_{abs}^* , I_{br}^* , I_{void}^* , and I_{inc}^*

$$\begin{cases} r = \sqrt{[\phi^k(\mathbf{x}, t)]^2 + [\psi(\mathbf{x}, t)]^2} \\ \theta = \tan^{-1} \left[\frac{\psi(\mathbf{x}, t)}{\phi^k(\mathbf{x}, t)} \right] \end{cases} \quad (9)$$

3. Basic formulation of XFEM

3.1 XFEM approximation

The XFEM approximation for 2D domains with cracks/voids/inclusions can be written as

$$\begin{aligned} \mathbf{u}^h(\mathbf{x}) = & \sum_{i \in I} N_i(\mathbf{x}) \mathbf{u}_i \\ & + \sum_{i \in I_{abs}^*} N_i^*(\mathbf{x}) [H(\mathbf{x}) - H(\mathbf{x}_i)] \mathbf{a}_i + \sum_{i \in I_{br}^*} N_i^*(\mathbf{x}) \sum_{j=1}^4 [F_j(\mathbf{x}) - F_j(\mathbf{x}_i)] \mathbf{b}_i^j \\ & + \sum_{i \in I_{void}^*} N_i^*(\mathbf{x}) [V(\mathbf{x}) - V(\mathbf{x}_i)] \mathbf{v}_i \\ & + \sum_{i \in I_{inc}^*} N_i^*(\mathbf{x}) [\varphi(\mathbf{x}) - \varphi(\mathbf{x}_i)] \mathbf{c}_i \end{aligned} \quad (10)$$

where $N_i(\mathbf{x})$ is the standard finite element shape function of node i ; \mathbf{u}_i is the unknown of the standard finite element part at node i ; I is the set of all nodes in the domain; $N_i^*(\mathbf{x})$ is the partition of unity functions, and the function can hold the same form with the standard finite element shape function but are not necessarily; \mathbf{a}_i , \mathbf{b}_i^j , \mathbf{v}_i , and \mathbf{c}_i is the nodal enriched degree of freedom; I_{abs}^* , I_{br}^* , I_{void}^* , and I_{inc}^* is the set of enrichment nodes shown in Fig. 4, and $I_{abs}^*, I_{br}^*, I_{void}^*, I_{inc}^* \subset I$.

For these elements which are cut completely by a crack, the nodes of these elements that are the nodal subset I_{abs}^* are enriched by Heaviside function $H(\mathbf{x})$. The definition of Heaviside function

$H(\mathbf{x})$ follows

$$H(\mathbf{x}) = \begin{cases} +1, & (\mathbf{x} - \mathbf{x}^*) \cdot \mathbf{n} > 0 \\ -1, & (\mathbf{x} - \mathbf{x}^*) \cdot \mathbf{n} < 0 \end{cases} \quad (11)$$

where, \mathbf{x}^* is the projection of a point \mathbf{x} on the crack surface; \mathbf{n} is the unit outward normal to the crack surface.

For these elements which are cut partially by a crack, the nodes of these elements that are the nodal subset I_{br}^* are enriched by the crack tip enrichment function $F_j(\mathbf{x})$. The definition of the crack tip enrichment function $F_j(\mathbf{x})$ follows

$$F_{j=1,2,3,4}(r, \theta) = \left\{ \sqrt{r} \sin \frac{\theta}{2}, \sqrt{r} \cos \frac{\theta}{2}, \sqrt{r} \sin \theta \sin \frac{\theta}{2}, \sqrt{r} \sin \theta \cos \frac{\theta}{2} \right\} \quad (12)$$

where r and θ are the local crack tip coordinate system.

For these elements which are cut by the interface of a void, the nodes of these elements that are the nodal subset I_{void}^* are enriched by the function $V(\mathbf{x})$ (Sukumar *et al.* 2001). If the node lies in the void, $V(\mathbf{x})=0$, or else $V(\mathbf{x})=1$.

For these elements which are cut by the interface of an inclusion, the nodes of these elements that are the nodal subset I_{inc}^* are enriched by the following function $\varphi(\mathbf{x})$ (Moës *et al.* 2003)

$$\varphi(\mathbf{x}) = \sum_{i \in I^*} N_i(\mathbf{x}) |\phi_i| - \left| \sum_{i \in I^*} N_i(\mathbf{x}) \phi_i \right| \quad (13)$$

3.2 Governing equations

Considering a bounded domain $\Omega \in R^2$, the boundary of the domain is partitioned into three parts, including the displacement boundary (Γ_u), traction boundary (Γ_t), and crack boundary (Γ_c) that is traction-free. According to the basic theory of elasto-statics, the equilibrium and boundary conditions for this problem may be described as

$$\begin{cases} \nabla \cdot \boldsymbol{\sigma} + \mathbf{b} = 0 & \text{in } \Omega \\ \boldsymbol{\varepsilon} = \nabla_s \mathbf{u} & \text{in } \Omega \\ \boldsymbol{\sigma} = \mathbf{D} : \boldsymbol{\varepsilon} & \text{in } \Omega \\ \boldsymbol{\sigma} \cdot \mathbf{n} = \bar{\mathbf{t}} & \text{on } \Gamma_t \\ \mathbf{u} = \bar{\mathbf{u}} & \text{on } \Gamma_u \\ \boldsymbol{\sigma} \cdot \mathbf{n} = 0 & \text{on } \Gamma_c \end{cases} \quad (14)$$

where $\boldsymbol{\sigma}$ is the Cauchy stress tensor, \mathbf{b} is the body force vector, $\boldsymbol{\varepsilon}$ is the strain tensor, ∇_s is the symmetric part of the gradient operator, \mathbf{u} is the displacement field vector, \mathbf{D} is the constitutive matrix, \mathbf{n} is the unit outward normal vector, $\bar{\mathbf{t}}$ is the external traction vector, and $\bar{\mathbf{u}}$ is the prescribed displacement.

3.3 Weak form

The admissible (trial) function space U is defined as

$$U = \{ \mathbf{u} \mid \mathbf{u} \in C^0, \mathbf{u} = \mathbf{u}_0 \text{ on } \Gamma_u, \text{ and } \mathbf{u} \text{ discontinuous on } \Gamma_u \} \quad (15)$$

The test function space V is defined as

$$V = \{ \mathbf{v} \mid \mathbf{v} \in C^0, \mathbf{v} = 0 \text{ on } \Gamma_u, \text{ and } \mathbf{v} \text{ discontinuous on } \Gamma_u \} \quad (16)$$

Hence, the weak form of the equilibrium equation can be described as: $\forall \mathbf{v} \in V$, find $\mathbf{u} \in U$, such that

$$\int_{\Omega} \boldsymbol{\sigma}(\mathbf{u}) : \boldsymbol{\varepsilon}(\mathbf{v}) d\Omega = \int_{\Omega} \mathbf{b} : \mathbf{v} d\Omega + \int_{\Gamma_t} \bar{\mathbf{t}} : \mathbf{v} d\Gamma \quad (17)$$

3.4 Discretized form

In this study, the XFEM program is implemented for the plane four nodes iso-parametric element. The approximating functions \mathbf{u}^h of the trial functions hold the same form with the approximating functions \mathbf{v}^h of the test functions \mathbf{v} . The functions \mathbf{u}^h and \mathbf{v}^h both satisfy Eq. (10). The weak form for the discrete problem can be stated as: find $\mathbf{u}^h \in V^h \subset V$, such that

$$\int_{\Omega} \boldsymbol{\sigma}(\mathbf{u}^h) : \boldsymbol{\varepsilon}(\mathbf{v}^h) d\Omega = \int_{\Omega} \mathbf{b} : \mathbf{v}^h d\Omega + \int_{\Gamma_t} \bar{\mathbf{t}} : \mathbf{v}^h d\Gamma \quad (18)$$

By substituting the trial and test functions in Eq. (18) and using the arbitrariness of the nodal variations, the following discrete equations can be obtained:

$$\mathbf{K}\boldsymbol{\delta} = \mathbf{R} \quad (19)$$

where \mathbf{K} is the global stiffness matrix assembled by the element stiffness matrix, $\boldsymbol{\delta}$ is the vector of nodal displacements, and \mathbf{R} is the global external force vector.

The element stiffness matrix can be expressed by

$$\mathbf{k}^e = \begin{bmatrix} \mathbf{k}^{uu} & \mathbf{k}^{ua} & \mathbf{k}^{ub} & \mathbf{k}^{uv} & \mathbf{k}^{uc} \\ \mathbf{k}^{au} & \mathbf{k}^{aa} & \mathbf{k}^{ab} & \mathbf{k}^{av} & \mathbf{k}^{ac} \\ \mathbf{k}^{bu} & \mathbf{k}^{ba} & \mathbf{k}^{bb} & \mathbf{k}^{bv} & \mathbf{k}^{bc} \\ \mathbf{k}^{vu} & \mathbf{k}^{va} & \mathbf{k}^{vb} & \mathbf{k}^{vv} & \mathbf{k}^{vc} \\ \mathbf{k}^{cu} & \mathbf{k}^{ca} & \mathbf{k}^{cb} & \mathbf{k}^{cv} & \mathbf{k}^{cc} \end{bmatrix} \quad (20)$$

where

$$\mathbf{k}^{rs} = \int_{\Omega^e} (\mathbf{B}^r)^T \mathbf{D} \mathbf{B}^s d\Omega = \int_{\Omega^e} \begin{bmatrix} \mathbf{B}_1^r & \mathbf{B}_2^r & \mathbf{B}_3^r & \mathbf{B}_4^r \end{bmatrix}^T \mathbf{D} \begin{bmatrix} \mathbf{B}_1^s & \mathbf{B}_2^s & \mathbf{B}_3^s & \mathbf{B}_4^s \end{bmatrix} d\Omega (r, s = u, a, b, v, c) \quad (21)$$

$$\mathbf{B}_i^u = \begin{bmatrix} \frac{\partial N_i}{\partial x} & 0 \\ 0 & \frac{\partial N_i}{\partial y} \\ \frac{\partial N_i}{\partial y} & \frac{\partial N_i}{\partial x} \end{bmatrix}, \quad i = 1, 2, 3, 4 \quad (22)$$

$$\mathbf{B}_i^a = \begin{bmatrix} \frac{\partial(N_i^* \hat{H})}{\partial x} & 0 \\ 0 & \frac{\partial(N_i^* \hat{H})}{\partial y} \\ \frac{\partial(N_i^* \hat{H})}{\partial y} & \frac{\partial(N_i^* \hat{H})}{\partial x} \end{bmatrix}, \quad \hat{H} = H(\mathbf{x}) - H(\mathbf{x}_i), \quad i = 1, 2, 3, 4 \quad (23)$$

$$\mathbf{B}_i^b = [\mathbf{B}_i^{b1} \quad \mathbf{B}_i^{b2} \quad \mathbf{B}_i^{b3} \quad \mathbf{B}_i^{b4}]$$

$$\mathbf{B}_i^{bj} = \begin{bmatrix} \frac{\partial(N_i^* \hat{F}_j)}{\partial x} & 0 \\ 0 & \frac{\partial(N_i^* \hat{F}_j)}{\partial y} \\ \frac{\partial(N_i^* \hat{F}_j)}{\partial y} & \frac{\partial(N_i^* \hat{F}_j)}{\partial x} \end{bmatrix}, \quad \hat{F}_j = F_j(\mathbf{x}) - F_j(\mathbf{x}_i), \quad i, j = 1, 2, 3, 4 \quad (24)$$

$$\mathbf{B}_i^v = \begin{bmatrix} \frac{\partial(N_i^* \hat{V})}{\partial x} & 0 \\ 0 & \frac{\partial(N_i^* \hat{V})}{\partial y} \\ \frac{\partial(N_i^* \hat{V})}{\partial y} & \frac{\partial(N_i^* \hat{V})}{\partial x} \end{bmatrix}, \quad \hat{V} = V(\mathbf{x}) - V(\mathbf{x}_i), \quad i = 1, 2, 3, 4 \quad (25)$$

$$\mathbf{B}_i^c = \begin{bmatrix} \frac{\partial(N_i^* \hat{\varphi})}{\partial x} & 0 \\ 0 & \frac{\partial(N_i^* \hat{\varphi})}{\partial y} \\ \frac{\partial(N_i^* \hat{\varphi})}{\partial y} & \frac{\partial(N_i^* \hat{\varphi})}{\partial x} \end{bmatrix}, \quad \hat{\varphi} = \varphi(\mathbf{x}) - \varphi(\mathbf{x}_i), \quad i = 1, 2, 3, 4 \quad (26)$$

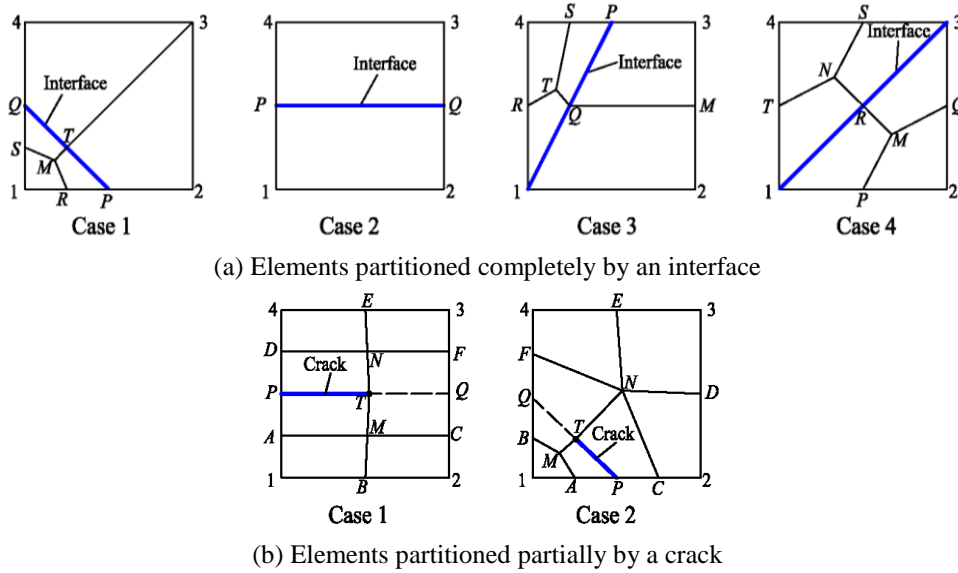


Fig. 5 Element partitioning method for these elements containing a discontinuous interface

The element external force vector is

$$\mathbf{r}^e = \left[\mathbf{r}^u \quad \mathbf{r}^a \quad \mathbf{r}^b \quad \mathbf{r}^v \quad \mathbf{r}^c \right]^T \tag{27}$$

where

$$\begin{cases} \mathbf{r}^u = \int_{\Omega^e} \mathbf{N}^T \mathbf{b} d\Omega + \int_{\Gamma_t^e} \mathbf{N}^T \bar{\mathbf{t}} d\Gamma \\ \mathbf{r}^a = \int_{\Omega^e} (\mathbf{N}^* \hat{\mathbf{H}})^T \mathbf{b} d\Omega + \int_{\Gamma_t^e} (\mathbf{N}^* \hat{\mathbf{H}})^T \bar{\mathbf{t}} d\Gamma \\ \mathbf{r}^{bj} = \int_{\Omega^e} (\mathbf{N}^* \hat{\mathbf{F}}_j)^T \mathbf{b} d\Omega + \int_{\Gamma_t^e} (\mathbf{N}^* \hat{\mathbf{F}}_j)^T \bar{\mathbf{t}} d\Gamma, \quad j=1,2,3,4 \\ \mathbf{r}^v = \int_{\Omega^e} (\mathbf{N}^* \hat{\mathbf{V}})^T \mathbf{b} d\Omega + \int_{\Gamma_t^e} (\mathbf{N}^* \hat{\mathbf{V}})^T \bar{\mathbf{t}} d\Gamma \\ \mathbf{r}^c = \int_{\Omega^e} (\mathbf{N}^* \hat{\varphi})^T \mathbf{b} d\Omega + \int_{\Gamma_t^e} (\mathbf{N}^* \hat{\varphi})^T \bar{\mathbf{t}} d\Gamma \end{cases} \tag{28}$$

3.5 Integration schemes at the discontinuities

For these elements partitioned by the boundary of an inclusion, a void, or a crack, the ordinary Gauss quadrature rules cannot accurately calculate the integration of enrichment function. The method subdividing the element into sub-quads is used. For these elements partitioned completely or partially by the boundary of an inclusion, a void, or a crack, the method subdividing these elements into sub-quads is shown in Fig. 5.

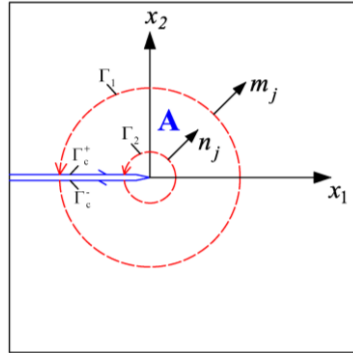


Fig. 6 Sketch map of the contour and domain integrals

4. Computation of SIF

Generally, the path-independent J -integral can be defined as follows (Rice 1968)

$$J = \lim_{\Gamma \rightarrow 0} \int_{\Gamma} (W \delta_{1j} - \sigma_{ij} u_{i,1}) n_j d\Gamma \tag{29}$$

where W is the strain energy density; the symbol δ_{ij} is Kronecker delta; and n_j is the outward normal vector to the contour Γ .

Take the field 1 $(\sigma_{ij}^{(1)}, \varepsilon_{ij}^{(1)}, u_i^{(1)})$ for the actual field, and the field 2 $(\sigma_{ij}^{(2)}, \varepsilon_{ij}^{(2)}, u_i^{(2)})$ for the auxiliary field. The choice for the auxiliary field is the asymptotical field of linear elastic fracture mechanics at the crack-tip, and the numerical results of the XFEM is chosen for the actual field. For the linear elastic problems, the J -integral can be used for the superposition of the actual and auxiliary fields, that is

$$J^{(1+2)} = \lim_{\Gamma \rightarrow 0} \int_{\Gamma} \left[\frac{1}{2} (\sigma_{ik}^{(1)} + \sigma_{ik}^{(2)}) (\varepsilon_{ik}^{(1)} + \varepsilon_{ik}^{(2)}) \delta_{1j} - (\sigma_{ij}^{(1)} + \sigma_{ij}^{(2)}) \frac{\partial (u_i^{(1)} + u_i^{(2)})}{\partial x_1} \right] n_j d\Gamma \tag{30}$$

Rewritten the Eq. (30), one can obtain the following formula

$$J^{(1+2)} = J^{(1)} + J^{(2)} + M^{(1,2)} \tag{31}$$

Naturally, $M^{(1,2)}$ is called the interaction integral, and it holds the following form

$$M^{(1,2)} = \lim_{\Gamma \rightarrow 0} \int_{\Gamma} (\sigma_{ik}^{(2)} \varepsilon_{ik}^{(1)} \delta_{1j} - \sigma_{ij}^{(2)} u_{i,1}^{(1)} - \sigma_{ij}^{(1)} u_{i,1}^{(2)}) n_j d\Gamma \tag{32}$$

Let the contour integral to be converted easily into a domain form, the Eq. (32) can be rewritten as

$$M^{(1,2)} = \lim_{\Gamma \rightarrow 0} \oint_{\Gamma_0} (\sigma_{ij}^{(1)} u_{i,1}^{(2)} + \sigma_{ij}^{(2)} u_{i,1}^{(1)} - \sigma_{ik}^{(2)} \varepsilon_{ik}^{(1)} \delta_{1j}) q m_j d\Gamma \tag{33}$$

where $\Gamma_0 = \Gamma_1 + \tilde{\Gamma}_2 + \Gamma_c^+ + \Gamma_c^-$ and $\tilde{\Gamma}_2$ is the opposite integral path of Γ_2 ; m_j is a unit outward

normal vector of the contour Γ_0 , evidently $m_j = -n_j$ on Γ_2 ; q is an arbitrary weight function with values varying smoothly from 1 on Γ_2 to 0 on Γ_1 ; see Fig. 6.

According to divergence theorem, the equivalent domain integral of Eq. (33) can be written as

$$M^{(1,2)} = \int_A \left(\sigma_{ij}^{(1)} u_{i,1}^{(2)} + \sigma_{ij}^{(2)} u_{i,1}^{(1)} - \sigma_{ik}^{(2)} \varepsilon_{ik}^{(1)} \delta_{1j} \right) \frac{\partial q}{\partial x_j} dA \quad (34)$$

where A is the circle domain with the center at the crack tip and the radius R . The radius R is defined as

$$R = r_k h_e \quad (35)$$

where h_e is the crack-tip element size; r_k is a user-specified scalar multiple, and here we set $r_k=2$. q is the weight function; if a node lies in the domain A , then $q=1$; else if the node is out of the domain A or lies in the boundary of the domain A , then $q=0$. In the interior of an element, the weight function q is obtained by the interpolation of the nodal value, that is

$$q = \sum_{i=1}^4 N_i q_i \quad (36)$$

The Eq. (34) can be expanded as

$$M^{(1,2)} = \int_A \left[\begin{aligned} & \left(\sigma_{11}^{(1)} u_{1,1}^{(2)} + \sigma_{12}^{(1)} u_{2,1}^{(2)} + \sigma_{11}^{(2)} u_{1,1}^{(1)} + \sigma_{21}^{(2)} u_{2,1}^{(1)} - \sigma_{11}^{(2)} \varepsilon_{11}^{(1)} - 2\sigma_{12}^{(2)} \varepsilon_{12}^{(1)} - \sigma_{22}^{(2)} \varepsilon_{22}^{(1)} \right) \frac{\partial q}{\partial x} \\ & + \left(\sigma_{12}^{(1)} u_{1,1}^{(2)} + \sigma_{22}^{(1)} u_{2,1}^{(2)} + \sigma_{12}^{(2)} u_{1,1}^{(1)} + \sigma_{22}^{(2)} u_{2,1}^{(1)} \right) \frac{\partial q}{\partial y} \end{aligned} \right] dA \quad (37)$$

Additionally, the interaction integral is related to SIF through the relation

$$M^{(1,2)} = \frac{2}{E^*} [K_I K_I^{\text{aux}} + K_{II} K_{II}^{\text{aux}}] \quad (38)$$

where K_I^{aux} and K_{II}^{aux} are the local auxiliary SIFs for the auxiliary fields, respectively; the definitions of E^* follows

$$E^* = \begin{cases} E & \text{(plane stress)} \\ \frac{E}{1-\nu^2} & \text{(plane strain)} \end{cases} \quad (39)$$

Setting $K_I^{\text{aux}} = 1$ and $K_{II}^{\text{aux}} = 0$, here $M^{(1,2)} = M_1^{(1,2)}$, we obtain the expression of K_I as follows

$$K_I = E^* M_1^{(1,2)} / 2 \quad (40)$$

Similarly, we can obtain

$$K_{II} = E^* M_2^{(1,2)} / 2 \quad (41)$$

by setting $K_I^{\text{aux}} = 0$ and $K_{II}^{\text{aux}} = 1$, here $M^{(1,2)} = M_2^{(1,2)}$.

5. Crack propagation criteria

The maximum circumferential stress criterion (Erdogan and Sih 1963) is used to determine the crack growth direction. Once K_I and K_{II} are calculated, the criterion gives the following crack growth direction

$$\theta_c = 2 \tan^{-1} \frac{1}{4} \left(\frac{K_I}{K_{II}} \pm \sqrt{\left(\frac{K_I}{K_{II}} \right)^2 + 8} \right) \quad (42)$$

where θ_c is the crack growth angle in the local crack-tip coordinate system. If $K_{II}=0$, then $\theta_c=0$. It should also be noted that if $K_{II}>0$, the crack growth angle $\theta_c<0$, and if $K_{II}<0$, then $\theta_c>0$. By a private communication with Suo, Sukumar and Prévost (2003) gives an improve expression for θ_c

$$\theta_c = 2 \tan^{-1} \left(\frac{-2K_{II}/K_I}{1 + \sqrt{1 + 8(K_{II}/K_I)^2}} \right) \quad (43)$$

The equivalent SIF then follows

$$K_e = \cos \frac{\theta_c}{2} \left(K_I \cos^2 \frac{\theta_c}{2} - 1.5 K_{II} \sin \theta_c \right) \quad (44)$$

If $K_e \geq K_{IC}$, then the crack grows, where K_{IC} is the material's fracture toughness.

6. Numerical verification

We have implemented the corresponding XFEM program by Fortran language in the environment of Microsoft Visual Stidio 2005. In this section, we mainly give several classic examples to verify the effectiveness of the implemented XFEM program.

6.1 Finite tensile plate with cracks

In this section, some of the basic problems of fracture mechanics with available analytical SIF solutions are illustrated. As shown in Fig. 7, the finite tensile plate problems that include an edge crack, a central crack, and double edge cracks will be considered. The plate with the width (b) of 1 m and the height (h) of 2 m is subjected to a tensile load (σ) of 1.0 kPa. The Young's modulus (E) of the plate is set to 1.0 MPa and Poisson's ratio (ν) is 0.2. The plane strain condition is assumed. In numerical model, the plate is discretized into a rectangular 59×119 meshes. To remove rigid body modes, appropriate displacement constraints are added.

For edge crack problem, available analytical SIF solutions are (Mohammadi 2008)

$$K_I = \left[1.12 - 0.23(a/b) + 10.56(a/b)^2 - 21.74(a/b)^3 + 30.42(a/b)^4 \right] \sigma \sqrt{\pi a} \quad (45)$$

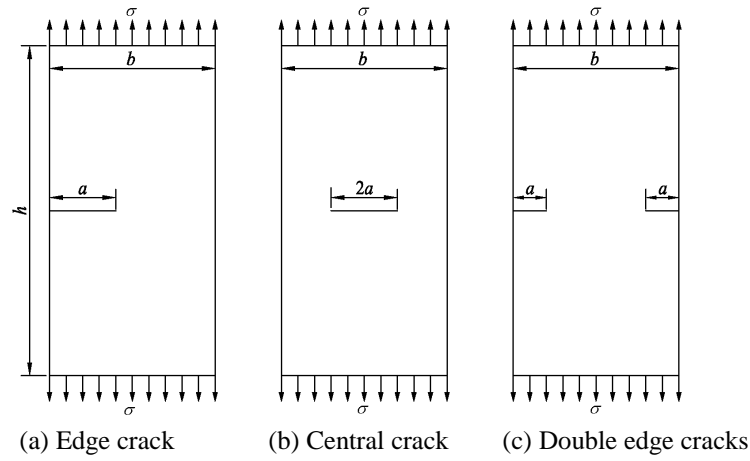


Fig. 7 Finite tensile plate problems

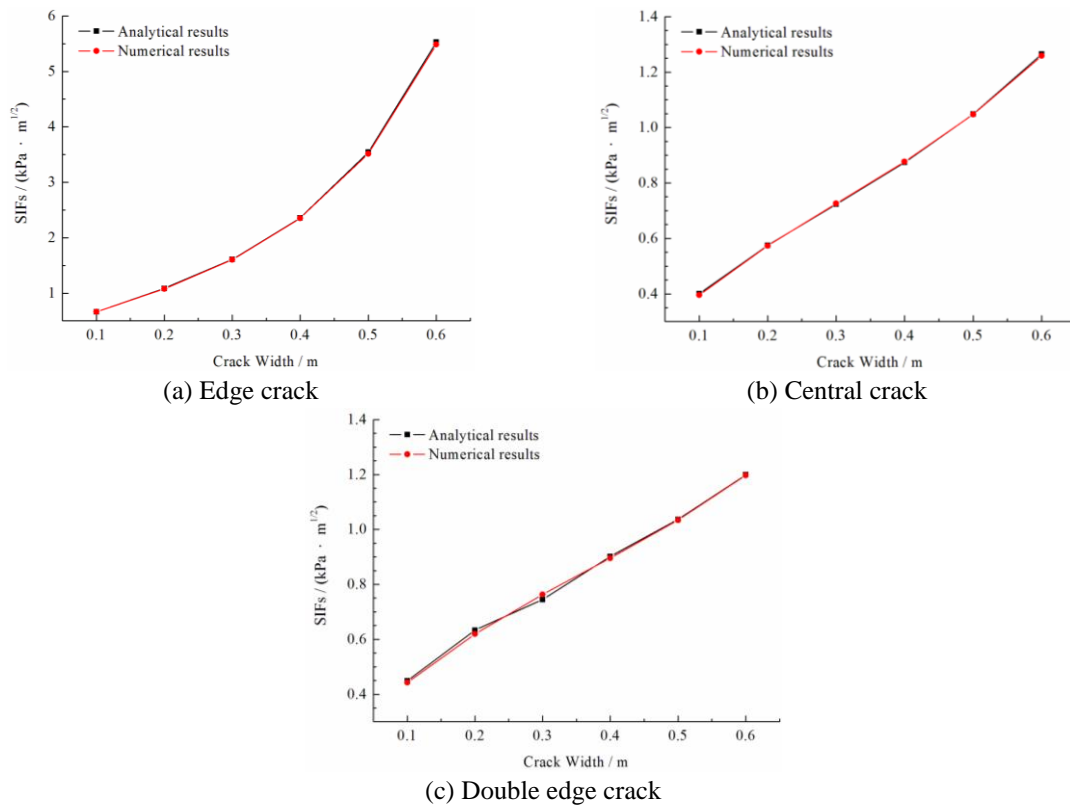


Fig. 8 Comparisons of numerical and analytical results for SIFs

For central crack problem, available analytical SIF solutions are (Mohammadi 2008)

$$K_I = \left[1 + 0.256(a/b) - 1.152(a/b)^2 + 12.2(a/b)^3 \right] \sigma \sqrt{\pi a} \quad (46)$$

For double edge crack problem, available analytical SIF solutions are (Mohammadi 2008)

$$K_I = \left[1.12 + 0.43(a/b) - 4.79(a/b)^2 + 15.46(a/b)^3 \right] \sigma \sqrt{\pi a} \quad (47)$$

Through the numerical analysis of the plate, it can be concluded that the numerical method yields an excellent agreement with the analytical solutions as shown in Fig. 8. This verification indicates that the implemented XFEM program in the paper is effective for the simulation of crack propagation.

6.2 A circle domain with a circle inclusion

As shown in Fig. 9, a circle domain with a radius of b is partitioned by its internal circular interface with a radius of a into two sub-domains Ω_1 and Ω_2 . On Ω_1 , the Lamé constants are $\lambda_1 = \mu_1 = 0.4$, and these on Ω_2 are $\lambda_2 = 5.7692$ and $\mu_2 = 3.8461$. These correspond to the elastic modulus $E_1 = 1$ Pa, $E_2 = 10$ Pa and Poisson ratio $\nu_1 = 0.25$, $\nu_2 = 0.3$. On Γ_2 , the prescribed displacement boundary conditions are $u_r = r$, $u_\theta = 0$. The plane strain conditions are assumed. In the numerical model, the plate in XFEM is discretized into 721 nodes and 684 elements, and the plate in FEM is discretized into 2265 nodes and 2204 elements.

The exact displacement solutions are (Sukumar *et al.* 2001)

$$\begin{cases} u_r(r) = \begin{cases} \left[(1 - b^2/a^2)\alpha + b^2/a^2 \right] r, & 0 \leq r \leq a \\ (r - b^2/r)\alpha + b^2/r, & a \leq r \leq b \end{cases} \\ u_\theta = 0 \end{cases} \quad (48)$$

where

$$\alpha = \frac{(\lambda_1 + \mu_1 + \mu_2)b^2}{(\lambda_2 + \mu_2)a^2 + (\lambda_1 + \mu_1)(b^2 - a^2) + \mu_2 b^2} \quad (49)$$

The numerical accuracy is investigated by the following equation

$$\text{err} = \sqrt{\frac{1}{NP} \sum_{i=1}^{NP} (u(\mathbf{x}_i) - u^h(\mathbf{x}_i))^2} / \sqrt{\frac{1}{NP} \sum_{i=1}^{NP} u^2(\mathbf{x}_i)}} \quad (50)$$

where NP is the number of nodes in the discretized domain; $u(\mathbf{x}_i)$ is the exact result at the point \mathbf{x}_i ; $u^h(\mathbf{x}_i)$ is the numerical result at the point \mathbf{x}_i .

Fig. 10 shows the numerical accuracy variation of XFEM for the problem against the number of nodes. With the increase of the number of nodes, the errors in the domain will decrease. The errors decrease from 1.40% to 1.02% with the increase of nodes from 505 nodes to 1561 nodes. Comparisons of the x -directional displacement/stress solutions in XFEM with those in FEM are presented in Fig. 11 and Fig. 12. The displacement solutions in FEM are completed by ABAQUS software. A satisfactory agreement can be observed. This verification indicates that the implemented XFEM program is effective for modeling inclusions.

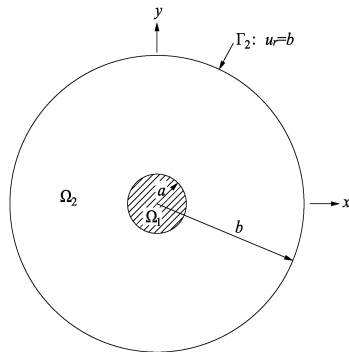


Fig. 9 A circle domain with a circle inclusion

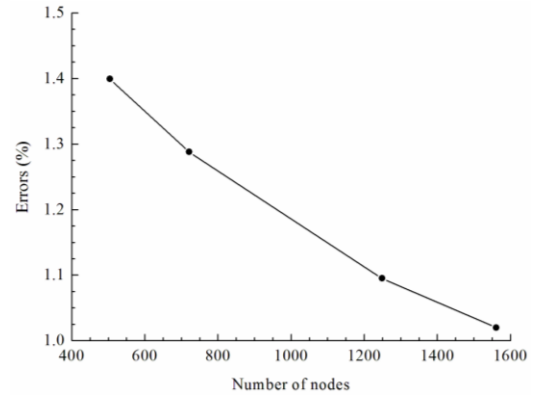


Fig. 10 Numerical accuracy variation for the problem with respect to the number of nodes

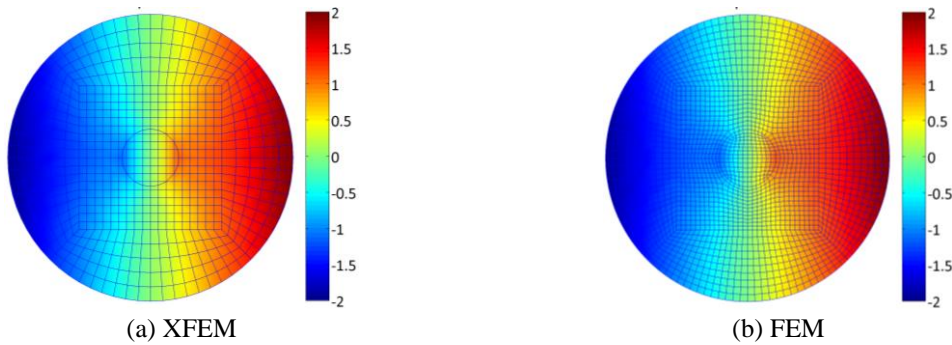


Fig. 11 Contour plot of the x -directional displacement / m

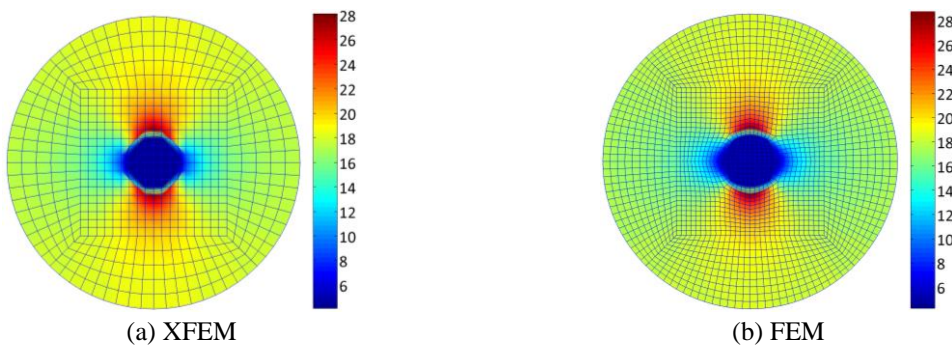


Fig. 12 Contour plot of the x -directional stress / Pa

6.3 A finite plate with a circle void

As shown in Fig. 13, a square plate with length (l) of 2 m contains a traction-free circular void with radius (r) of 0.4 m at its center. The plate is subjected to a uniaxial tension load (σ) of 1000 Pa. The plane strain condition is assumed. The Young's modulus (E) of the plate is set to 100000 Pa and Poisson's ratio (ν) is 0.3. In the numerical model, the plate in XFEM is discretized into

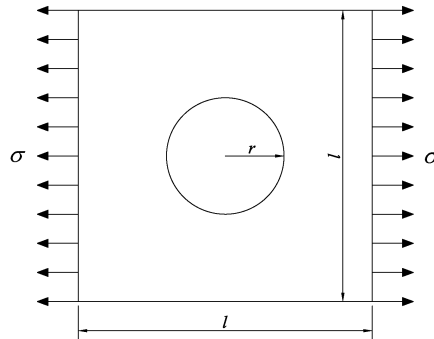
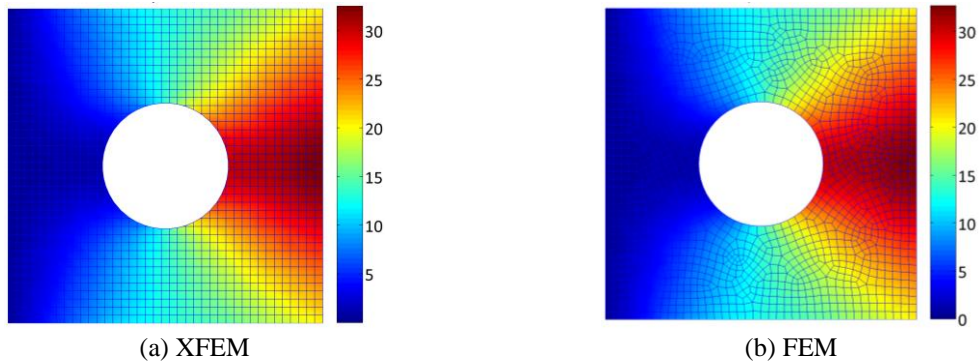
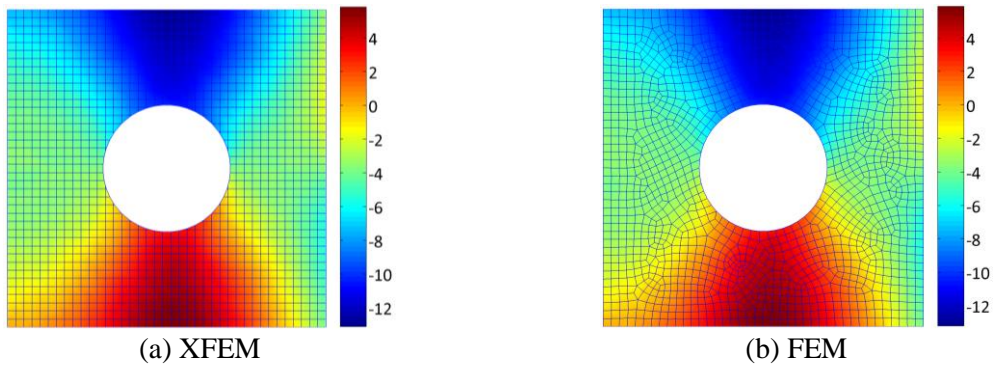


Fig. 13 A square plate with a traction-free circular hole

Fig. 14 Contour plot of the x -directional displacement / mmFig. 15 Contour plot of the y -directional displacement / mm.

39×39 meshes of 4-node quadrilateral elements, with 1600 nodes and 1521 elements, and in FEM, the plate is discretized into 1669 nodes and 1564 elements. To remove rigid body modes, appropriate displacement constraints are added.

Comparisons of the displacement solutions in XFEM with those in FEM are presented in Fig. 14 and Fig. 15. The displacement solutions in FEM are completed by ABAQUS software. A perfect agreement can be observed. This verification indicates that the implemented XFEM program in the paper is effective for modeling voids.

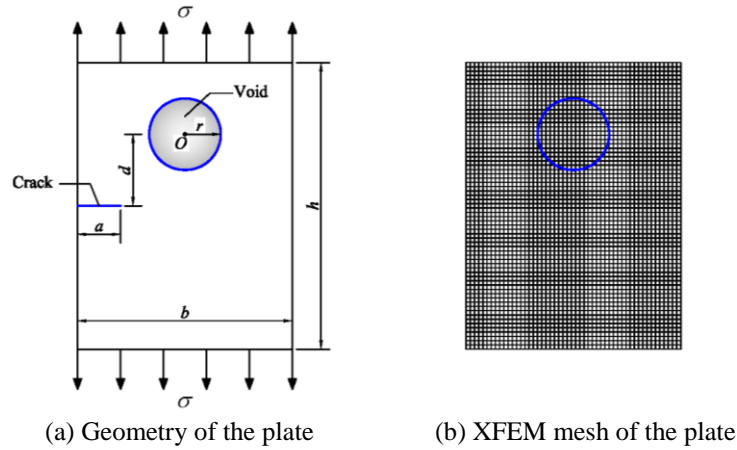


Fig. 16 A plate with an edge crack and a circular void / mm

7. Numerical examples

7.1 Crack path deflection because of voids

As shown in Fig. 16(a), a plate with an edge crack and a circular void of radius (r) is considered. The width (b) of the plate is set to be 15 mm and the height (h) is set to be 20 mm. The plate is subjected to uniform tension load (σ) of 1000 MPa at its top and bottom edges. The matrix material is assumed to be purely elastic. The matrix material properties are the Young's modulus (E) of 98,000 MPa and Poisson's ratio (ν) of 0.3. The plane stress condition is assumed. Thickness of the plate is set to be 1 mm. The value of K_{IC} is assumed to be 1000 N/mm^{3/2} in this study. In numerical model, the plate is discretized into 67×50 meshes of 4-node quadrilateral elements with 3648 nodes and 3350 elements shown in Fig. 16(b).

In this section, we investigate the effects of the location, dimension, and quantity of void on the path of crack propagation. As shown in Fig. 17, keeping the radius (r) at 2.5 mm, the effects of the distance (d) varying from 4.0 mm to 6.0 mm on the final predicted crack paths are observed. The distance between the center of the void and the left edge of the plate is 7.5 mm. The crack propagates into the void when the distance (d) equals to 4.0 mm. With the increase of the distance (d), the crack initially curves towards the void, then, the crack reorients itself and propagates almost horizontally along width of the plate.

Additionally, we also observe the effects of the radius (r) varying from 2.0 mm to 3.0 mm on the final predicted crack paths while keeping the distance (d) at 5.0 mm. The distance between the center of the void and the left edge of the plate is 7.5 mm. The crack propagates into the void when the radius (r) equals to 3.0 mm. With the decrease of the radius (r), the crack initially curves towards the void, then, the crack reorients itself and propagates almost horizontally along width of the plate.

In Fig. 19, we change the quantity of voids from one to three, but the ratio of voids remains unchanged. For the plate containing a void, the radius of the void is set to be 2.5 mm. The distance between the center of the void and the left edge of the plate is 7.5 mm. For the plate containing two voids, the radius of each void is set to be 1.768 mm. The distance between the center of the first (second) void and the left (right) edge of the plate is 5.0 mm. For the plate containing three

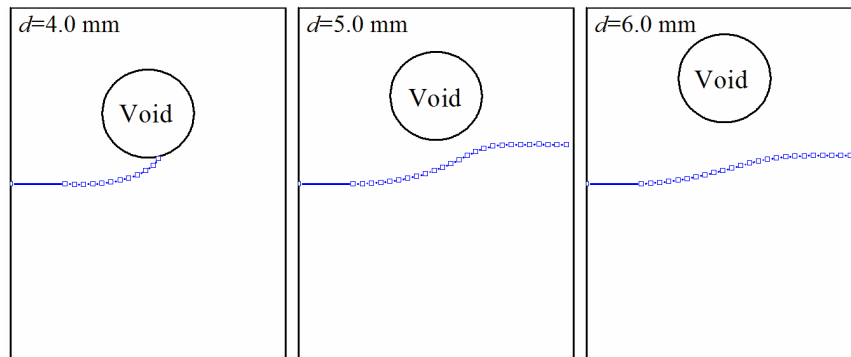


Fig. 17 Final predicted crack paths of the plate with a void under different distances d ($r=2.5$ mm)

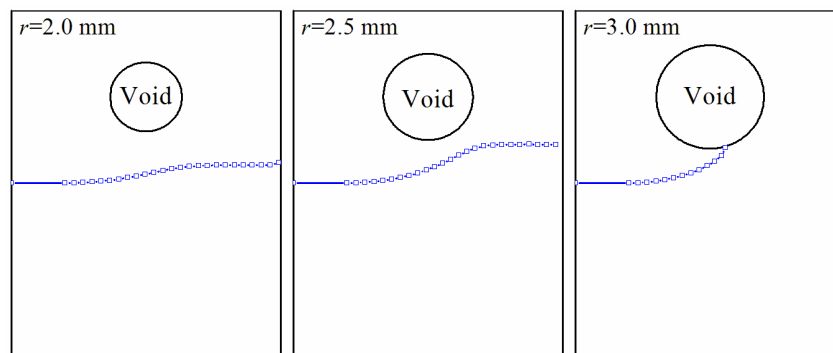


Fig. 18 Final predicted crack paths of the plate with a void under different radius r ($d=5$ mm)

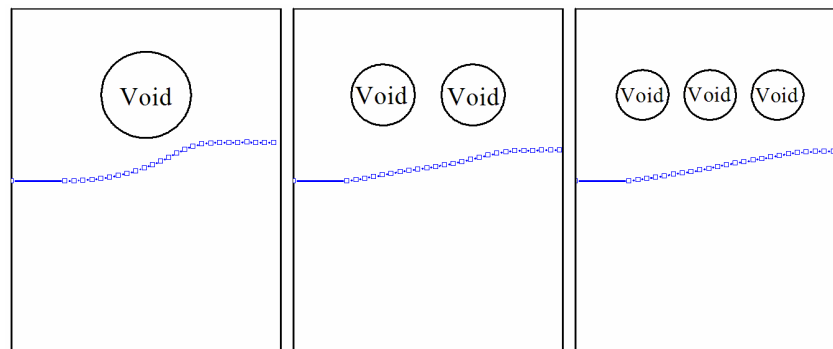


Fig. 19 Final predicted crack paths of the plate with different void's quantity

voids, the radius of each void is set to be 1.443 mm. The distance between the center of the first (third) void and the left (right) edge of the plate is 3.75 mm. From the figure, we still can observe that the crack initially curves towards the void, then, the crack reorients itself and propagates almost horizontally along width of the plate.

For the plate containing cracks and voids, two possibly crack path can be observed: i) the crack propagates into the void with a bigger void size or a closer distance between the void and the crack; ii) with a smaller void size or a far distance between the void and the crack, the crack

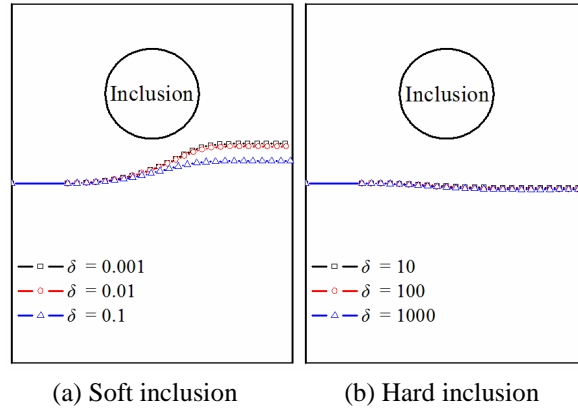


Fig. 20 Effects of inclusion properties on the final predicted crack paths

initially curves towards the void, then, the crack reorients itself and propagates along its original orientation.

7.2 Crack path deflection because of inclusions

In this section, we mainly investigate the effects of the inclusion on the path of crack propagation. The geometric dimensions, material properties, the load conditions, and the boundary conditions of the plate both are identical with these described in section 7.1, but the plate contains an inclusion instead of a void. The Young's modulus (E') of the inclusion varies from 98 MPa to 98,000,000 MPa, and its Poisson's ratio (ν') keeps at 0.3. In numerical model, the XFEM mesh is identical with the mesh given in Fig. 16(b). Defining $\delta = E'/E$, as shown in Fig. 20, keeping the radius (r) of 2.5 mm and the distance (d) of 5.0 mm, the effects of inclusion properties on the final predicted crack paths are mainly concerned. As δ varying from 0.001 to 0.1 with a soft inclusion, the final predicted crack paths tend to close with the inclusion. As δ varying from 10 to 1000 with a hard inclusion, the final predicted crack paths tend to away from the inclusion. An evident difference of crack paths can be observed as δ varying from 0.001 to 0.1 with a soft inclusion. However, as δ varying from 10 to 1000, a slightly difference of crack paths can only be seen.

7.3 Crack path deflection because of minor cracks

In this section, we mainly investigate the effects of the minor cracks on the path of major crack propagation. The geometric dimensions, material properties, the load conditions, and the boundary conditions of the plate both are identical with these described in section 7.1, but the plate contains several minor cracks with no propagation apart from a major crack. In numerical model, the XFEM mesh is identical with the mesh given in Fig. 16(b). Fig. 21 show several distribution models of minor cracks in the plate.

As shown in Fig. 22, the final predicted major crack paths for the plate with several distribution models of minor cracks are given. No matter what distribution models of minor cracks, the trend of major crack paths can still be described as that the crack initially curves towards the minor cracks, then, the crack reorients itself and propagates almost horizontally along width of the plate.

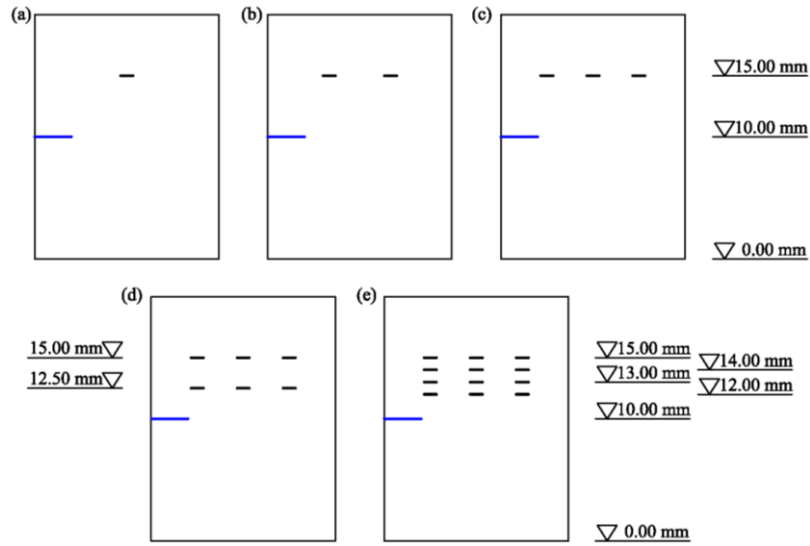


Fig. 21 Several distribution models of minor cracks in the plate, (a) the plate with one minor crack; (b) the plate with two minor cracks; (c) the plate with three minor cracks; (d) the plate with six minor cracks; (e) the plate with twelve minor cracks

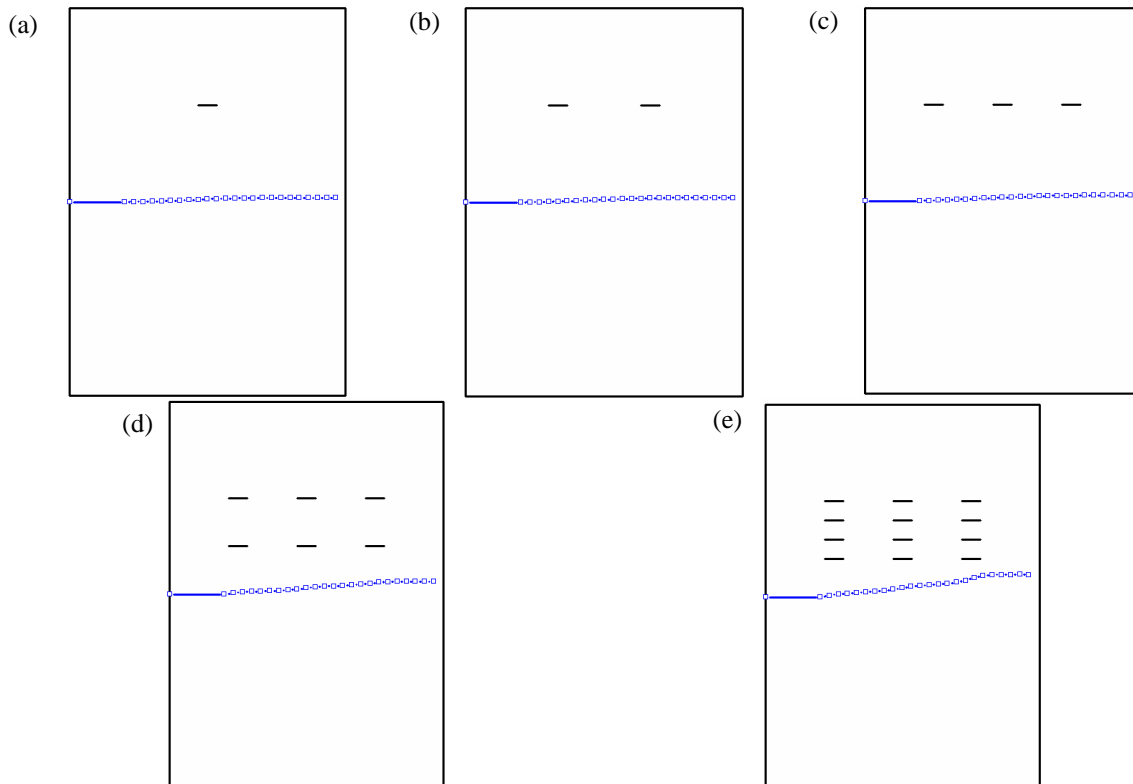


Fig. 22 The final predicted major crack paths for the plate with several distribution models of minor cracks, (a) the plate with one minor crack; (b) the plate with two minor cracks; (c) the plate with three minor cracks; (d) the plate with six minor cracks; (e) the plate with twelve minor cracks

8. Conclusions

For structures containing multiple discontinuities (voids, inclusions, and cracks), the simulation technologies in the framework of XFEM are discussed in details. The emphasis are paid on the selections of enrichment functions, the numerical integrations at the discontinuities, the evaluations of SIF, as well as the criterion of crack propagation. The LSM is used for representing the location of inner discontinuous interfaces containing the boundaries of voids and inclusions, and the surface of cracks, so that the mesh does not need to align with these discontinuities. The governing equation for XFEM is deduced. Several illustrations have been given to verify that the implemented XFEM program is effective for modeling voids, inclusions, and crack propagation. Then, the implemented XFEM program is used to investigate the effects of the voids, inclusions, and minor cracks on the path of major crack propagation. The following conclusions can be drawn:

For a plate containing cracks and voids, two possibly crack path can be observed: i) the crack propagates into the void; ii) the crack initially curves towards the void, then, the crack reorients itself and propagates along its original orientation.

For a plate with a soft inclusion, the final predicted crack paths tend to close with the inclusion, and an evident difference of crack paths can be observed with different inclusion material properties. However, for the plate with a hard inclusion, the paths tend to away from the inclusion, and a slightly difference of crack paths can only be seen with different inclusion material properties.

For a plate with several minor cracks, the trend of major crack paths can still be described as that the crack initially curves towards the minor cracks, then, the crack reorients itself and propagates almost horizontally along width of the plate.

Acknowledgements

The authors gratefully acknowledge support for this research from the National Natural Science Foundation of China (Grant Nos. 51309088, 11372098, 11132003 and 51139001), China Postdoctoral Science Foundation funded project (Grant No. 2013M530233), and Jiangsu Planned Projects for Postdoctoral Research Funds (Grant No. 1301112C).

References

- Belytschko, T. and Black, T. (1999), "Elastic crack growth in finite elements with minimal remeshing", *Int. J. Numer. Meth. Eng.*, **45**(5), 601-620.
- Dréau, K., Chevaugeon, N., Moës, N. (2010), "Studied X-FEM enrichment to handle material interfaces with higher order finite element", *Comput. Method. Appl. Mech. Eng.*, **199**, 1922-1936.
- Du, C.B, Jiang, S.Y., Qin, W., Xu, H. and Lei, D. (2012), "Reconstruction of internal structures and numerical simulation for concrete composites at mesoscale", *Comput. Concrete*, **10**(2), 135-147.
- Erdogan, F. and Sih, G.C. (1963), "On the crack extension in plane loading and transverse shear", *J. Basic Eng.*, **85**, 519-527.
- Haboussa, D., Grégoire, D., Elguedj, T., Maigre, H. and Combescure, A. (2011), "X-FEM analysis of the effects of holes or other cracks on dynamic crack propagations", *Int. J. Numer. Method. Eng.*, **86**, 618-636.

- Kim, J., Zi, G., Van, S.N., Jeong, M.C., Kong, J.S. and Kim, M.S. (2011), "Fatigue life prediction of multiple site damage based on probabilistic equivalent initial flaw model", *Struct. Eng. Mech.*, **38**(4), 443-457.
- Liao, J.H. and Zhuang, Z. (2012), "A Lagrange-multiplier-based XFEM to solve pressure Poisson equations in problems with quasi-static interfaces", *SCIENCE CHINA Phys., Mech. Astron.*, **55**(4), 693-705.
- Mayer, U.M., Popp, A., Gerstenberger, A. and Wall, W.A. (2010), "3D fluid-structure-contact interaction based on a combined XFEM FSI and dual mortar contact approach", *Comput. Mech.*, **46**, 53-67.
- Melenk, J.M. and Babuška, I. (1996), "The partition of unity finite element method: basic theory and applications", *Comput. Method. Appl. Mech. Eng.*, **39**, 289-314.
- Moës, N., Cloirec, M., Cartraud, P. and Remacle, J.F. (2003), "A computational approach to handle complex microstructure geometries", *Comput. Method. Appl. Mech. Eng.*, **192**(28-30), 3163-3177.
- Mohammadi, S. (2008), *Extended finite element method*, Blackwell Publishing Ltd, Oxford, UK.
- Osher, S. and Sethian, J.A. (1988), "Fronts propagating with curvature-dependent speed: algorithms based on Hamilton-Jacobi formulations", *J. Comput. Phys.*, **79**(1), 12-49.
- Rice, J.R. (1968), "A path independent integral and the approximate analysis of strain concentrations by notches and cracks", *J. Appl. Mech.*, **35**, 379-386.
- Singh, I.V., Mishra, B.K., Bhattacharya, S. and Patil, R.U. (2012), "The numerical simulation of fatigue crack growth using extended finite element method", *Int. J. Fatigue*, **36**, 109-119.
- Singh, I.V., Mishra, B.K. and Bhattacharya, S. (2011), "XFEM simulation of cracks, holes and inclusions in functionally graded materials", *Int. J. Mech. Mater. Des.*, **7**, 199-218.
- Stolarska, M. and Chopp, D.L. (2003), "Modeling thermal fatigue cracking in integrated circuits by level sets in the extended finite element method", *Int. J. Numer. Method. Eng.*, **41**, 2381-2410.
- Sukumar, N., Chopp, D.L., Moës, N. and Belytschko, T. (2001), "Modeling holes and inclusions by level sets in the extended finite element method", *Comput. Method. Appl. Mech. Eng.*, **190**(46-47), 6183-6200.
- Sukumar, N. and Prévost, J.H. (2003), "Modeling quasi-static crack growth with the extended finite element method, Part I: Computer implementation", *Int. J. Solid. Struct.*, **40**, 7513-7537.
- Sun, H., Waisman, H. and Betti, R. (2013), "Nondestructive identification of multiple flaws using XFEM and a topologically adapting artificial bee colony algorithm", *Int. J. Numer. Method. Eng.*, **95**, 871-900.
- Wu, Z.J. and Wong, L.N.Y. (2013), "Modeling cracking behavior of rock mass containing inclusions using the enriched numerical manifold method", *Eng. Geol.*, **162**, 1-13.
- Yan, Y. and Park, S. (2008), "An extended finite element method for modeling near-interfacial crack propagation in a layered structure", *Int. J. Solid. Struct.*, **45**, 4756-4765.
- Ye, C., Shi, J. and Cheng, G.J. (2012), "An eXtended Finite Element Method (XFEM) study on the effect of reinforcing particles on the crack propagation behavior in a metal-matrix composite", *Int. J. Fatigue*, **44**, 151-156.